Sensors & Actuators: B. Chemical 382 (2023) 133479

Contents lists available at ScienceDirect

Sensors and Actuators: B. Chemical

journal homepage: www.elsevier.com/locate/snb

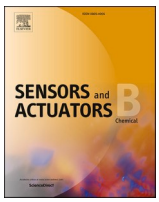

A split-type photoelectrochemical immunosensor based on a high-performance $In_2O_3/BiVO_4$ photoelectrode modulated by a ZIF-8 protective layer

Yu Bai [a], Dongquan Leng [a], Tao Feng [a], Xuan Kuang [a], Dawei Fan [a], Xiang Ren [a], Yuyang Li [a,*], Qin Wei [a,b,**], Huangxian Ju [a,c]

[a] Collaborative Innovation Center for Green Chemical Manufacturing and Accurate Detection, Key Laboratory of Chemical Sensing & Analysis in Universities of Shandong, School of Chemistry and Chemical Engineering, University of Jinan, Jinan 250022, China
[b] Department of Chemistry, Sungkyunkwan University, Suwon 16419, the Republic of Korea
[c] State Key Laboratory of Anal. Chem. for Life Science, Department of Chemistry, Nanjing University, Nanjing 210023, China

ARTICLE INFO

Keywords:
Split-type
Photoelectrochemical immunosensors
$In_2O_3/BiVO_4$
ZIF-8
Glucose oxidase

ABSTRACT

Herein, a split-type photoelectrochemical (PEC) immunosensor is designed to detect neuron-specific enolase (NSE), which is a tumor marker for small cell lung cancer present in nerve and neuroendocrine tissues. In this study, a heterogeneous $In_2O_3/BiVO_4$ structure is developed with coral-like $BiVO_4$ films adsorbed onto In_2O_3 based on simplified successive ionic layer adsorption and reaction (s-SILAR). Moreover, immune recognition occurs in a 96-well plate in the split-type PEC immunosensor, thus effectively avoiding interference with the recognition of biomolecules. However, the sensitivity of zeolitic imidazolate framework (ZIF)− 8 molecules to pH varies, and most of the degradation of ZIF-8 molecules can be achieved by a reaction at a pH of 5.5–6.5 for > 30 min. Therefore, SiO_2-glucose oxidase is selected as a regulatory switch to act on ZIF-8 molecules by catalyzing the conversion of glucose to gluconic acid, whereas $In_2O_3/BiVO_4$ is selected as the photoactive substrate and ZIF-8 protective layer as the signal switch. By constructing a split-type PEC immunosensor, gluconic acid of different concentrations is released in the 96-well plate through the change of NSE concentration to regulate the degradation of the ZIF-8 protective layer and achieve the sensitive detection of NSE. The constructed PEC sensor exhibits an excellent photocurrent response between 0.1 pg mL^{-1} and 100 ng mL^{-1}, with a detection limit of 0.03 pg mL^{-1}. Simultaneously, the accuracy, specificity, stability, and reproducibility of this split-type PEC sensing platform predict its promising application in the future in the field of biomolecules.

1. Introduction

Biosensors have been gradually applied in food, environmental detection, and clinical medicine industries owing to their rapid development [1–3]. Photoelectrochemical (PEC) immunosensors, a novel biosensor, are favored because of their high specificity, sensitivity, and stability; thus, they have significantly changed the traditional immunoassay method and integrated the advantages of traditional immunoassays with biosensor technologies [4,5]. PEC immunosensors reduce analysis time, enhance assay precision and specificity, and simplify the determination procedure and automation; thus, they are suitable for a wide range of applications [6]. Recently, several attempts have been made to detect biometric elements, such as antibodies, aptamers, cells, bionics, and cells or tissues, using traditional PEC immunosensors [7,8]. Clinical studies have shown that neuron-specific enolase (NSE) is a valuable molecular marker in clinical applications. This is based on two aspects of applications: first, NSE can be used as a tumor marker for lung cancer and pediatric neuroblastoma for the differential diagnosis of small cell lung cancer (SCLC) and non–SCLC and for monitoring the disease, treatment response, and prediction of recurrence of SCLC and neuroblastoma; second, changes in NSE activity are closely associated with several neurological disorders caused by nerve damage [9–11]. In

* Corresponding author.
** Corresponding author at: Collaborative Innovation Center for Green Chemical Manufacturing and Accurate Detection, Key Laboratory of Chemical Sensing & Analysis in Universities of Shandong, School of Chemistry and Chemical Engineering, University of Jinan, Jinan 250022, China.
E-mail addresses: chm_liyy@ujn.edu.cn (Y. Li), sdjndxwq@163.com (Q. Wei).

https://doi.org/10.1016/j.snb.2023.133479
Received 4 October 2022; Received in revised form 31 January 2023; Accepted 4 February 2023
0925-4005/© 2023 Elsevier B.V. All rights reserved.

this study, NSE present in the enolase of the glycolysis pathway of nerve tissue and neuroendocrine tissue was employed to investigate the PEC immunosensor.

The photoactive component is an integral part of PEC immunosensor construction [12]. In recent decades, heterostructures with interleaved energy levels have been extensively implemented during the fabrication of PEC immunosensor platforms owing to their distinct photoelectric conversion properties, which facilitate the arrangement of photogenerated electron–hole pairs and are beneficial for the transfer of photogenerated carriers [13,14]. Indium oxide, a representative *n*-type semiconductor, has an indirect bandgap of approximately 2.8 eV and is often used as a photocatalytic active material owing to its excellent photostability. Although a single In_2O_3 does not respond vigorously to light energy, the photoelectric signal is typically amplified by a composite heterogeneous structure [15,16]. As is well known, heterojunction interfaces can be formed between semiconductors with matching band potential in composite semiconductor materials. Compared with other materials, several Bi^{3+}-based semiconductors have excellent visible-light activity because of their suitable conduction band (CB) and valence band (VB) positions owing to the hybridization of O 2p and Bi 6 s^2 [17]. Monoclinic $BiVO_4$ is an *n*-type semiconductor with several oxidation active sites and a bandgap of approximately 2.3–2.4 eV. It possesses a wide visible-light absorption range and outstanding PEC capability when irradiated with visible light; hence, it has advanced significantly in the PEC sensing industry [18]. Heterojunction interfaces can be constructed between semiconductors with matching band potentials; thus, the electric charge generated by the light can be transferred from one semiconductor to another. This is advantageous for the separation of photoelectrons and holes, which can significantly improve the photoelectric performance of semiconductor heterostructures. Note that the bandgap of $BiVO_4$ ($E_g = 2.4$ eV) is lower than that of In_2O_3 ($E_g = 2.8$ eV); however, the VB of In_2O_3 ($E_{VB} = 2.17$ eV *vs.* normal hydrogen electrode (NHE)) is lower than that of $BiVO_4$ ($E_{VB} = 2.75$ eV *vs.* NHE). Essentially, the energy levels of In_2O_3 and $BiVO_4$ are well matched to combine the photogenerated carriers to form highly efficient heterostructures that enable the separation of the photogenerated carriers [19–22].

Metal-organic frameworks (MOFs) have broad application prospects in gas storage, drug delivery, catalysis, and chemical sensors [23–25]. Zeolitic imidazolate frameworks (ZIFs) are porous crystal materials in which an organic imidazole ester is crosslinked to the transition metal to form a tetrahedral framework [26]. However, ZIF molecules typically exhibit unsatisfactory electrical conductivity, and bulk organic ligands typically block electron transport. Nonetheless, they are extremely sensitive to acidic environments, and subtle changes in pH under acidic conditions produce different degradation assemblies for ZIF molecules [27,28]. In acidic media, the time required to decompose the ZIF-8 protective layer at different pH values is an important factor to consider [29]; the slow decomposition of ZIF-8 occurs at pH $\leq$ 6.5 [30]. Chen et al. determined that ZIF-8 could not be completely broken down when exposed to 50 mM gluconic acid for 1 h [31]. Liang et al. demonstrated that the degradation of ZIF-8 was not only dependent on pH changes but also on time [32].

A conventional sandwich-type PEC immunosensor typically requires the biomaterial to be directly modified on the photoactive material; this not only affects the sensitivity of the detected substance but increases the accidental error of the sensor when the number of modified layers is excessively high [33,34]. The split-type PEC immunosensor separates the construction of photoelectric active substrate materials from the immune recognition process, thus avoiding direct contact with the heterogeneous semiconductor material and improving the sensitivity of the sensor. Moreover, in practical applications, it is consistent with the need for bioconjugation process detection, which is the focus of current studies [35,36].

Therefore, this study designed a split-type PEC immunosensor with an In_2O_3 photoactive substrate and prepared an indium tin oxide (ITO)/In_2O_3/$BiVO_4$ heterostructure electrode using simplified successive ionic layer adsorption and reaction (s-SILAR) [37]. The ITO/In_2O_3/$BiVO_4$ was covered with a protective layer of ZIF-8; however, the poor electrical conductivity of the ZIF material hindered electron transport. Hence, SiO_2-loaded glucose oxidase (GOx) was introduced as a bioconjugate of Ab_2 during immunization, where changes in the NSE concentration released different concentrations of gluconic acid to break the protective layer of ZIF-8 and restore the photoelectric signal. Furthermore, a semiconductor/MOF-based material was designed for split-type PEC immunosensors [38,39]. Split-type PEC immunosensors exhibit a high sensitivity, low detection limit, wide detection range, and good selectivity and specificity, thus enabling further investigation of the PEC immunosensor detection of NSE.

2. Experimental section

2.1. Preparation of In_2O_3/$BiVO_4$

In_2O_3/$BiVO_4$ with $BiVO_4$ monoclinic films were adsorbed on In_2O_3 nanoparticles by a simplified SILAR (s-SILAR) method (more details are provided in the Supplementary Material (SM)) [40]. First, 25 mM Bi $(NO_3)_3$ was dissolved in 20 mL of a mixture of acetic acid and water at room temperature (acetic acid:water, 1:19 v/v) as the Bi source, and 25 mM NH_4VO_3 was dissolved in 20 mL at room temperature in a V bath. The ITO electrode, coated with 10 μL of 5 mg mL^{-1} In_2O_3, was immersed in a Bi bath for 20 s, washed in ultrapure water, immersed in a V bath for 20 s, and washed again in ultrapure water for one s-SILAR cycle. After 20 cycles, the samples were annealed at 450 °C for 2 h at a rate of 10 °C min^{-1}. Other details of the reagents and apparatus are provided in the SM.

2.2. Fabrication of the PEC immunosensor

As shown in Scheme 1A, an on-off-on sandwich immunosensor was established based on PEC signals. Before use, the ITO electrode was ultrasonicated using acetone, ethanol, and ultrapure water for 30–40 min, and then dried under nitrogen. In particular, 10 μL of a homogeneous suspension of 5 mg mL^{-1} In_2O_3 was dropped onto the ITO electrode. After drying, the ITO/In_2O_3/$BiVO_4$ electrode was obtained using the s-SILAR method (refer the SM). Subsequently, 10 μL of the ZIF-8 electrostatic protective layer was modified on the ITO/In_2O_3/$BiVO_4$ electrode. The prepared ITO/In_2O_3/$BiVO_4$/ZIF-8 electrode was maintained at 4 °C overnight.

The immunization process of the split-type system is described in detail in Scheme 1B. Immunization was performed in 96-well plates. First, 1 μg mL^{-1} of the Ab_1 stock solution was injected into a 96-well plate. The cells were incubated overnight at 4 °C to ensure that Ab_1 grew in the 96-well plate. Subsequently, the cells were washed with phosphate-buffered saline (PBS). To minimize accidental errors, the micropores were washed with PBS for each subsequent incubation; then, 100 μL 1 wt% Bovine serum albumin (BSA) was added and incubated for 1 h at 37 °C to close the nonspecific binding site. Next, 100 μL of different concentrations of NSE antigens were placed in the 96-well plates and incubated at 37 °C for 1 h. After washing the unbound NSE with PBS, 100 μL of GOx-SiO_2-Ab_2 bioconjugate was added and incubated at 37 °C for 1 h, followed by repeated washing. Finally, 100 μL 20 mM glucose solution was added to96-well pate and maintained at room temperature for 30 min as a further assay for the split-type PEC immunosensor. the degradation effect of the protective layer of ZIF-8 was observed in gluconic acid solution and the gluconic acid solution was incubated in 10 μL of the protective layer of ZIF-8 for 5, 10, 20, and 30 min. As can be observed in Fig. S1, the ZIF-8 crystal pattern deteriorated after 30 min. To further illustrate the sensitivity of the ZIF-8 layer to glucose acidity, gluconic acid with different pH values were employed to incubate the ZIF-8 protective layer. Fig. S2 shows that the desired degradation of the ZIF-8 protective layer can be achieved with a pH of

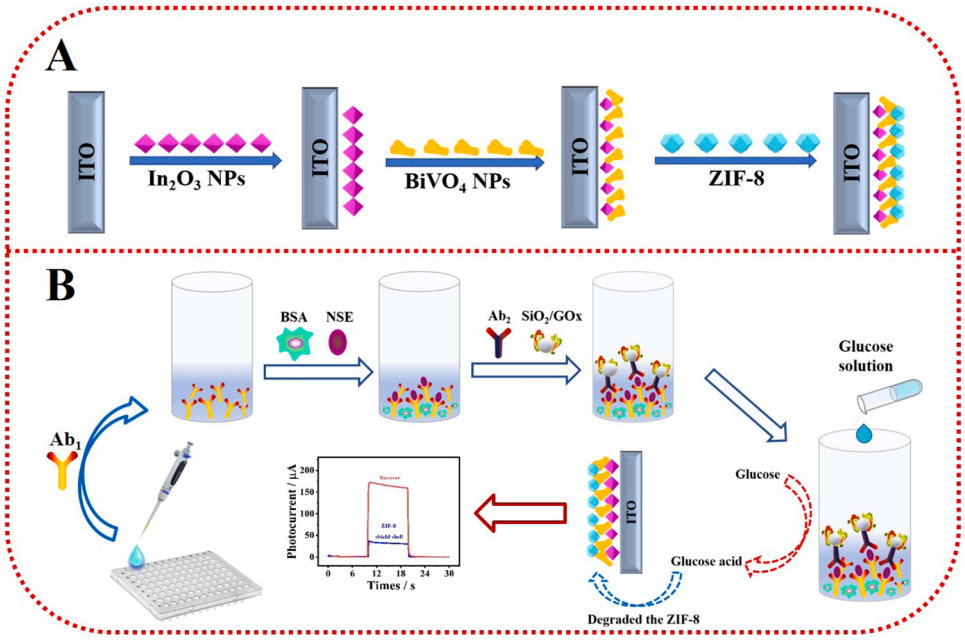

Scheme 1. (A) Preparation of $In_2O_3/BiVO_4$/ZIF-8 electrode; and (B) split-type PEC immunosensor fabrication procedure for NSE detection.

6.5 and incubation time of 30 min

2.3. PEC detection in a split-type immunosensor

PEC measurements were performed using a PEC workstation with an excitation light source of a 100 mW cm^{-2} light-emitting diode lamp with white light irradiation using a three-electrode system in 0.12 M ascorbic acid (AA). The transient photocurrent method was used. A voltage of 0 V was applied, and the lamp was switched on and off every 10 s to obtain the time–photocurrent curve. The wavelengths of the light sources are shown in Fig. S3.

3. Results and discussion

3.1. Characterization of nanomaterials

The micromorphology and microstructure of the electrode based on In_2O_3 were observed using scanning electron microscopy (SEM). Fig. 1 A shows the microscopic morphology of the In_2O_3 nanoparticles; evidently, the electrode comprised small nanoparticles with diameters of approximately 40 nm. Fig. 1B shows the transmission electron microscopy (TEM) image of In_2O_3. According to the high-resolution (HR)-TEM results, the 110 crystal plane of the In_2O_3 nanoparticles was 0.2636 nm. Fig. 1 C shows the $BiVO_4$ layers grown on the In_2O_3 nanoparticles using the s-SILAR method. Evidently, the $BiVO_4$ layer was coral-like, and the HR-TEM images of $BiVO_4$ in Fig. 1D revealed that the lattice length of $BiVO_4$ was 0.3086 nm, corresponding to the 121 crystal plane. A simple ZIF-8 coating is shown in Fig. 1E, essentially exhibiting regular cubes. The SiO_2 microspheres exhibited good bioadaptability, and the size of the SiO_2 shown in Fig. 1 F was approximately 200 nm. The X-ray diffraction (XRD) pattern of the layer-modified electrode is shown in Fig. 1 G. By analyzing the diffraction patterns of In_2O_3, the 2θ angles were observed to be 22.376°, 30.993°, 32.618°, 45.618°, 50.255°, 57.205°, and 58.194°, corresponding to its (012), (104), (110), (024), (116), (214), and (300) crystal planes, respectively (JCDS card no. 22–0336). Thus, the compounded $In_2O_3/BiVO_4$ layer successfully compounded the $BiVO_4$ layer while maintaining its original crystal structure. Evidently, the 2θ angles were 18.669°, 28.947°, 30.548°, 39.782°, and 53.310°, corresponding to the (110), (121), (040), (211), and (161) crystal planes of $BiVO_4$, respectively (JCDS card no. 14–0688). The $In_2O_3/BiVO_4$/ZIF-8 composite layer (011), (002), (112), and (222) crystal planes were compared with the standard ZIF-8 card shown in Fig. S4. The UV–visible absorption (Fig. 1H) peak of pure In_2O_3 was observed at approximately 300 nm, whereas that of the complex heterojunction, $In_2O_3/BiVO_4$, was at approximately 450 nm, essentially extending the absorption range of visible light. Further, the $In_2O_3/BiVO_4$ nanocomposite was characterized by X-ray photoelectron spectroscopy (XPS) to determine the compound composition and chemical state of the samples (Fig. 1I).

The XPS spectrum of In 3d (Fig. S5B) exhibited two peaks, at 452.5 and 444.5 eV, denoting In $3d_{5/2}$ and In $3d_{3/2}$, respectively, which is characteristic of In^{3+} in In_2O_3. Bi 4 $f_{5/2}$, Bi 4 $f_{7/2}$, V $2p_{1/2}$, and V $2p_{3/2}$ (Figs. S5C and D) exhibited peaks at 164.5, 158.5, 524.5, and 516.9 eV, respectively, which are consistent with the previously reported peak locations of Bi^{3+} and V^{5+} in $BiVO_4$. The three fitted peaks at binding energies (BEs) of 532.1, 531.2, and 530.3 eV in O 1 s were be attributed to the adsorbed water, surface hydroxyl groups, and lattice oxygen, respectively. Furthermore, the O 1 s peak exhibited a high BE peak at 529.6 eV, corresponding to the lattice oxygen of the oxide, and the BE shoulder peak at 532 eV was attributed to the surface hydroxide [41]. The results indicate that the $In_2O_3/BiVO_4$ composite nanomaterial heterojunction contained In_2O_3 and $BiVO_4$.

The effective electrode surface area was improved by introducing a $BiVO_4$ load on the In_2O_3 surface. This disordered coral-like $BiVO_4$ membrane is key to establishing electron transport and amplifying the PEC signal with a faster electron mobility. Thus, cyclic voltammerty (CV) of In_2O_3 and $In_2O_3/BiVO_4$ in the $[Fe(CN)_6]^{4-/3-}$ solution was performed [42]. The redox peak current, I, was related to $v^{1/2}$ according to the Randles–Sevcik equation, $I = 2.69 \times 10^5 AD^{1/2}n^{3/2}v^{1/2}c$, where A denotes the effective electroactive surface area (cm^2), D is the diffusion coefficient of $[Fe(CN)_6]^{4-/3-}$, $n = 1$, v denotes the scanning rate (V s^{-1}), and $c = 5$ mM (concentration of $K_3Fe(CN)_6$). At scanning rates ranging from 20 to 240 mV s^{-1} (Fig. 2 A and B) shows a good linear relationship. The calculated effective electroactive surface areas of In_2O_3 and $In_2O_3/BiVO_4$ were 0.44 and 0.59 cm^2, respectively, increasing by approximately 34%. To evaluate the electrocatalytic performance of $In_2O_3/BiVO_4$, CV measurements were recorded using 0.12 mM AA. Fig. 2 C shows the measured CV curve, where $In_2O_3/BiVO_4$ exhibited a high current response in PBS (pH = 7.4). The photocatalytic activity of $In_2O_3/BiVO_4$ was evaluated under various lighting conditions (Fig. 2D).

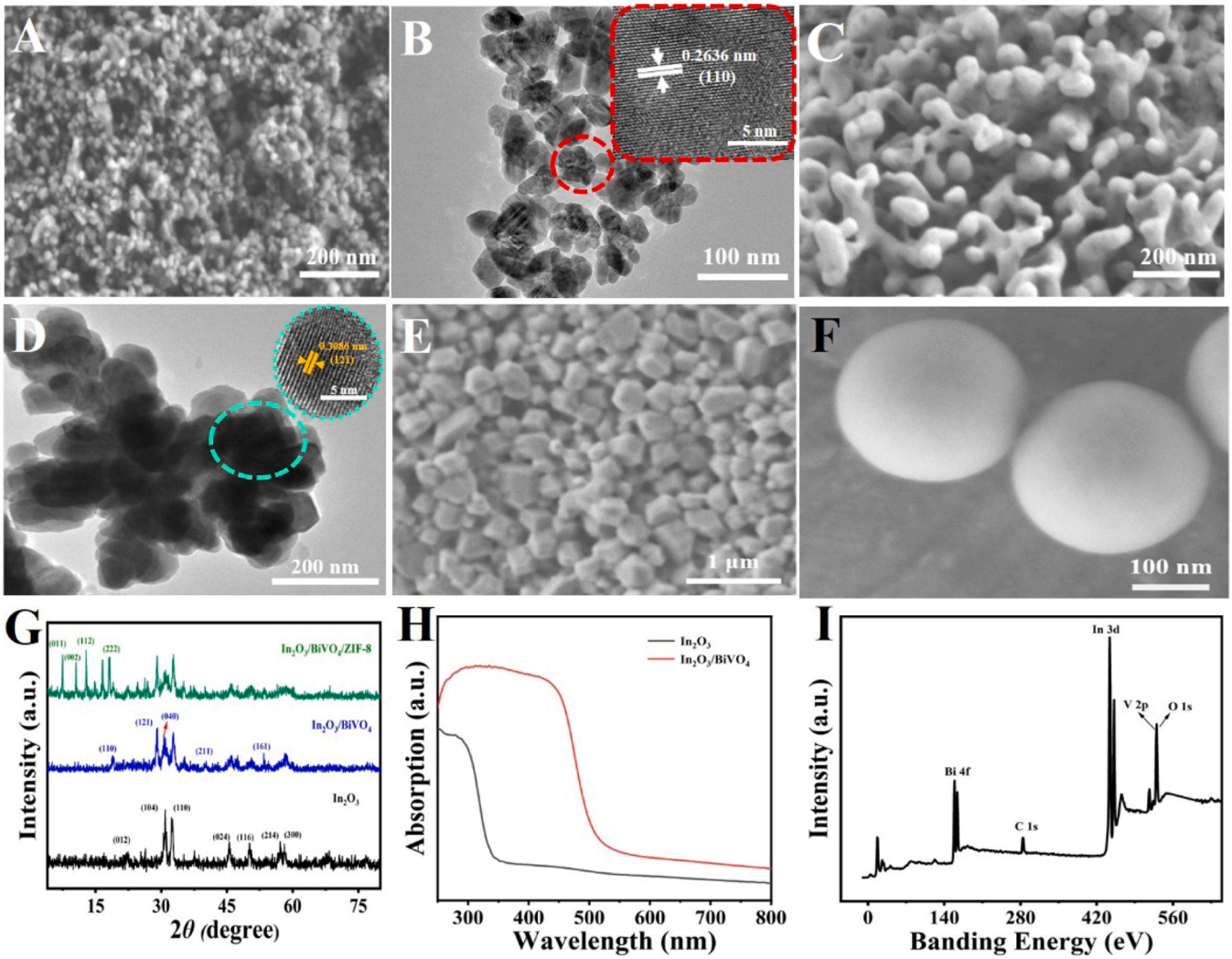

Fig. 1. (A) SEM image of In_2O_3. (B) Transmission electron microscopy (TEM) image of In_2O_3 (inset is a high-resolution TEM (HR-TEM) image of In_2O_3). (C) Scanning electron microscopy (SEM) image of $BiVO_4$. (D) TEM image of $BiVO_4$ (inset is the HR-TEM image of $BiVO_4$). (E) SEM image of ZIF-8 protective shell. (F) SEM image of SiO_2. (G) X-ray diffraction (XRD) patterns of In_2O_3, $In_2O_3/BiVO_4$, and $In_2O_3/BiVO_4$/ZIF-8. (H) Ultraviolet–visible (UV–vis) absorption spectra of In_2O_3 and $In_2O_3/BiVO_4$. (I) X-ray photoelectron spectroscopy (XPS) survey spectrum of $In_2O_3/BiVO_4$ full heterostructures.

Evidently, $In_2O_3/BiVO_4$ exhibited a high current response ($\Delta I = 60$ μA) under light exposure. Subsequently, photoluminescence spectroscopy was conducted to confirm the charge-recombination detainment capability of the constructed heterojunction (Fig. S6A). In contrast to the original In_2O_3, a sharp, intense transition zone was observed near 520 and 680 nm, and the band strength of $In_2O_3/BiVO_4$ was weak, thus suggesting that *in situ* engineered heterojunctions ($In_2O_3/BiVO_4$) can significantly decrease the interfacial charge carrier recombination [43–45]. As shown in Fig. S6B, the electron spin resonance (ESR) signal of the·O^{2-} free radical generated by the $In_2O_3/BiVO_4$ samples was the highest under visible-light irradiation, whereas the ESR signal could barely be observed under dark conditions, thus indicating that·O^{2-} free radicals can generate PEC reaction systems at room temperature. The untransported electrons of $In_2O_3/BiVO_4$ catalyzed the formation of superoxide, whereas the consumption of AA as an electron donor prevented the recombination of electron-hole pairs. Thus, charge-carrier recombination were found to be minimized.

3.2. PEC layer modification of split-type PEC sensors

To confirm the successful fabrication of the split-type PEC sensor, the material was modified layerwise on the electrode to measure the photocurrent signal response, and the impedance value was an effective method of monitoring the change in the electrode interface qualities. As shown in Fig. 3 A, the PEC signal of the empty ITO electrode was nearly 0 μA (curve a). After the photosensitive material, In_2O_3 was lower, and a lower photocurrent signal appeared (curve b). Subsequently, a layer of $BiVO_4$ thin film was adsorbed on In_2O_3 using the s-SILAR method, whereas a strong PEC signal appeared in curve c. When the ZIF-8 precursor solution was dropped onto the ITO/$In_2O_3/BiVO_4$ electrode, the PEC signal decreased significantly (curve d). When the released gluconic acid degraded ZIF-8, the photoelectric signal was restored (curve e).

Electrochemical impedance spectroscopy (EIS) was conducted in a 5.0 mM $[Fe(CN)_6]^{3-/4-}$ solution containing 0.1 M KCl, and the results are shown in Fig. 3B. The Randall equivalent circuit is denoted by a Nyquist diagram, including the electron-transfer resistance, R_{et}, solution resistance, Rs, Varburg impedance, $Z\omega$, and double-layer capacitance, C_{dl}, shown in the inset of Fig. 3B, whose values are presented in Table S1 (fitted with ZSimpwin). Evidently, the naked ITO electrode exhibited the lowest R_{et} value (Fig. 3B (curve a)). The impedance value gradually increased with a decrease in the In_2O_3 content (curve b). Subsequently, $BiVO_4$ films were adsorbed in In_2O_3 by the s-SILAR method, which led to a further increase in the electrochemical impedance owing to the inherent poor conductivity of the semiconductor (curve c). A significant

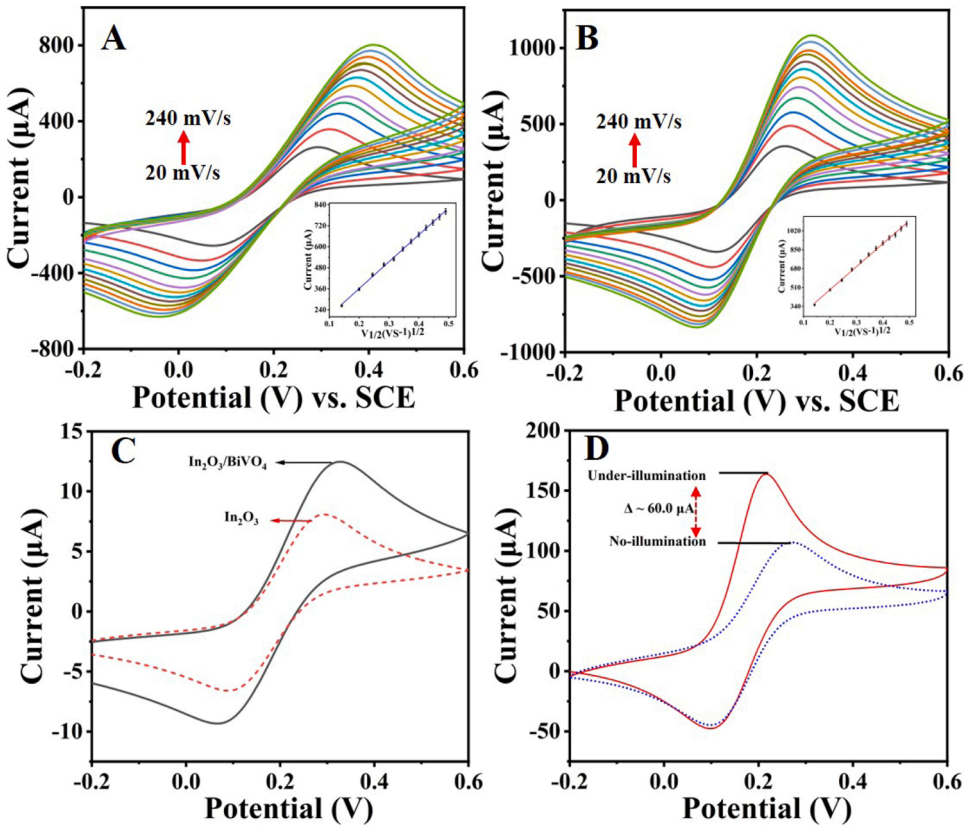

Fig. 2. (A) Cyclic voltammetry (CV) curves of ITO/In_2O_3 electrodes at scan rates of 20–240 mV s^{-1} (inset shows the calibration curve of *I vs.* $v^{1/2}$). (B) CV curves of ITO/In_2O_3/$BiVO_4$ electrodes at scan rates of 20–240 mV s^{-1} (inset shows the calibration curve of *I vs.* $v^{1/2}$). (C) Cyclic voltammograms of the ITO/In_2O_3 and ITO/In_2O_3/$BiVO_4$ in 0.1 M PBS solution. (D) Electrocatalytic oxidation of AA (0.12 M) using ITO/In_2O_3/$BiVO_4$ both under illuminated and nonilluminated conditions.

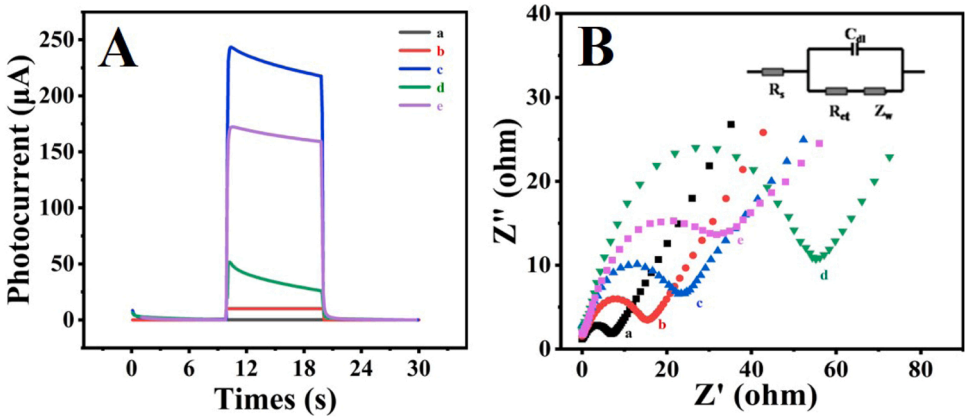

Fig. 3. (A) Photocurrent curve and (B) electrochemical impedance spectroscopy Nyquist plots for: (a) ITO electrode, (b) ITO/In_2O_3, (c) ITO/In_2O_3/$BiVO_4$, (d) ITO/In_2O_3/$BiVO_4$/ZIF-8, and (e) after the release of gluconic acid in the ITO/In_2O_3/$BiVO_4$/ZIF-8 electrode. The inset in (B) is the Randles equivalent circuit for EIS.

impedance was generated after adding the ZIF-8 protective layer, which hindered electron transfer more than the semiconductor (curve d). With the addition of gluconate, the ZIF-8 protective layer gradually decomposed and the impedance value decreased (curve e). Thus, using these phenomena, a split-type PEC immunosensor was successfully constructed.

3.3. Optimization of experimental conditions

To obtain better performance of the split-type sensor, its advantages were fully utilized and some conditions, such as the In_2O_3 concentration, number of cycles of ion layer adsorption, concentration of AA, and incubation time, were optimized.

As shown in Fig. 4A, the effect of the concentration of substrate In_2O_3 on the photoelectric signal, ranging from 3.0 to 10.0 mg mL^{-1}, was investigated. The photocurrent exhibited an increasing trend when the concentration was < 5.0 mg mL^{-1} and the peak value appeared at 5.0 mg mL^{-1}, thus indicating that the sensor had the best performance when the concentration of In_2O_3 was 5.0 mg mL^{-1}. The $BiVO_4$ thin film prepared by the s-SILAR method needs to be cycled in Bi and V baths for a certain number of times, which can then significantly improve the photocurrent of In_2O_3. The photocurrent intensity of the In_2O_3/$BiVO_4$ heterostructure under different cycle times was investigated; evidently, the ITO/In_2O_3/$BiVO_4$ electrode exhibited an unexpected photocurrent

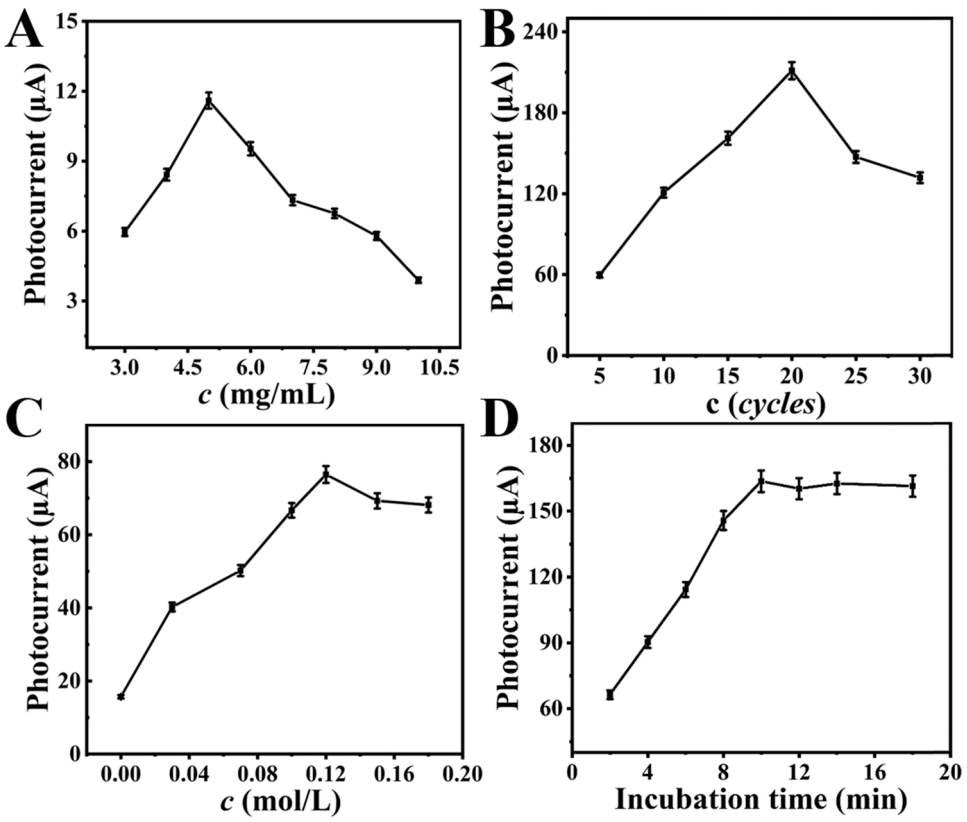

Fig. 4. Optimization of experimental conditions. (A) In_2O_3 concentration, (B) number of cycles of s-SILAR, (C) AA concentration in the PBS, and (D) incubation time of glucose. Error bars = SD ($n = 3$).

intensity after 20 cycles (Fig. 4B). To further explore the effect of the concentration variation on the optimal performance, a more detailed exploration of the In_2O_3 concentration and $BiVO_4$ cycle number was performed (Fig. S8). Evidently, an In_2O_3 concentration of 5 mg mL^{-1} and s-SILAR cycle number of 20 were determined to be the optimal conditions. The protective ZIF-8 layer was synthesized using a simple method. To further explore the conditions for the formation of the protective layer of ZIF-8, the molar ratios of the mixed solutions were explored and the molar ratios of 2-methylimidazole and zinc acetate dihydrate solutions were selected to be 1:1, 2:1, 3:1, 4:1, and 5:1 for conditional screening. As can be observed in Fig. S9, the protective ZIF-8 layer worked best when the molar ratio was 4:1. AA could trap photogenerated holes and prevent photogenerated electron–hole pairs from recombination as electron donors. When the AA concentration was 0.12 M, the $In_2O_3/BiVO_4$/ZIF-8 temporal current reached its maximum (Fig. 4C). The optimal incubation time was selected to measure the performance of the modified PEC immunosensor by testing the degradation of the ZIF-8 layer by gluconic acid generated from a GOx-catalyzed glucose solution. When the photocurrent reached its maximum, the catalytic time was 10 min (Fig. 4D).

3.4. PEC detection for NSE

A possible mechanism of the constructed split-type sensor electron transport is illustrated in Fig. 5. Type-II heterojunctions are well-known to significantly contribute to the excitation of photoelectric activity. Herein, in the type-II heterojunction, the energy bands of the two semiconductors were staggered. Electrons migrated from the CB of

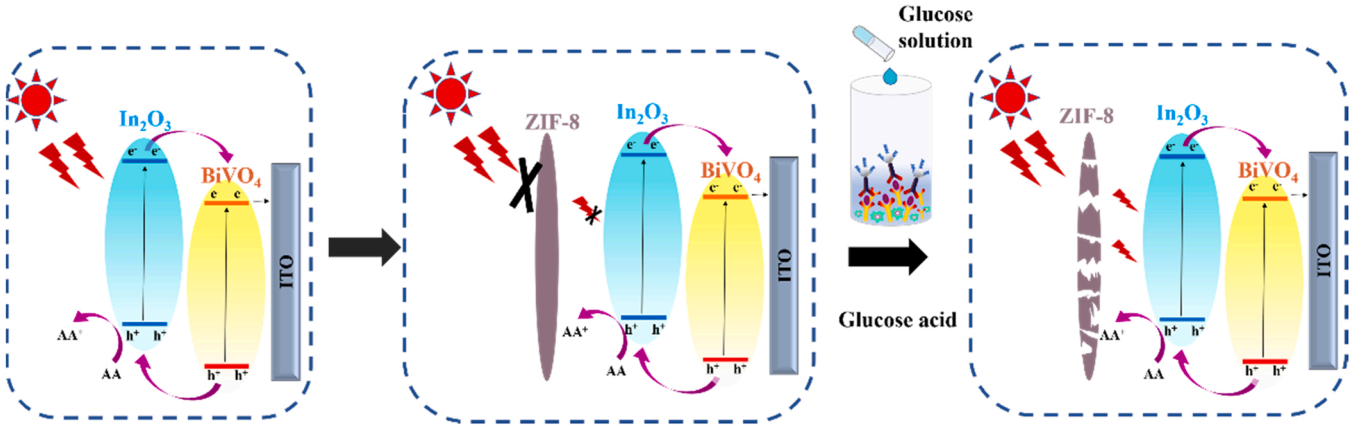

Fig. 5. Split-type PEC immunosensor potential mechanism of e^-/h^+ transfer for NSE detection. The applied potential was 0 V.

semiconductor 1 to the CB of semiconductor 2, where they accumulated. Whereas holes migrated from the VB of semiconductor 2 to the VB of semiconductor 1 and accumulated on semiconductor 1, thereby achieving effective separation of electrons and holes in space; note that the CB and VB of $BiVO_4$ are more negative than those of In_2O_3. The UV–vis diffuse reflectance spectra of In_2O_3 and $BiVO_4$ are shown in Figs. S7A and B, and their bandgap energies were calculated to be 2.8 and 2.4 eV, respectively. The slope of the Mott–Schottky curve can determine the type of semiconductor material. As can be observed in Figs. S7C and D, In_2O_3 and $BiVO_4$ are *n*-type semiconductors. Furthermore, the Mott–Schottky curves indicated that the flat band potentials of In_2O_3 and $BiVO_4$ were –0.82 and 0.11 V *vs.* the saturated calomel electrode (–0.58, 0.35 V *vs.* NHE). Based on this data and $Eg = E_{VB} - E_{CB}$, E_{VB} of In_2O_3 and $BiVO_4$ were 2.22 and 2.75 V *vs.* NHE, respectively. Because the In_2O_3 and $BiVO_4$ films had matching cascade band-edge values, the photocurrent intensity could be efficiently increased by preventing the compounding of the photogenerated electron–hole pairs. Under visible-light irradiation, the photogenerated electrons were excited from the VB of In_2O_3 to the CB, and the excited electrons were then transferred from the CB of In_2O_3 to the VB of $BiVO_4$, which prevented the recombination of photogenerated electron–hole pairs. Simultaneously, the photogenerated holes were finally transferred to the VB of In_2O_3 and trapped by AA. After the ZIF-8 protective layer was dripped onto the modified working electrode, the excitation of photogenerated electrons was hindered, the transmission of electrons was hindered owing to its large steric hindrance, and the distance of electronic transmission was increased. Upon the addition of glucose acid released by the immune process, the ZIF-8 protective layer began degrading owing to its sensitivity to pH. The $In_2O_3/BiVO_4$ heterostructure was then photosensitized again, and the excited carrier transport process and photoelectric signal were restored.

The constructed split-type PEC immunosensor was employed to detect NSE and the photocurrent response was directly related to the concentration of the detected substance. Fig. 6 A shows the photocurrents at different concentrations. With an increase in the concentration of the measured substance, the photocurrent improved continuously because the higher the NSE concentration, the more GOx was transported in the 96-well plate, and the gluconic acid released could effectively decompose the ZIF-8 protective layer to achieve the recovery of the photocurrent. Accordingly, a good linear relationship between the photocurrent and NSE concentration was observed between 0.1 pg mL^{-1} to 100 ng mL^{-1}, as shown in Fig. 6B, which provided a good mathematical basis for our detection. The formula of linear fitting was $I = 136.77 + 23.90 \log c$ and the coefficient of linear correlation $R^2 = 0.9967$. Furthermore, the split-type PEC immunosensor exhibited a detection limit of 0.03 pg mL^{-1} ($S/N = 3$). The wider detection range and lower detection limit of other PEC immunosensors detecting NSE are listed in Table S2 and S3. Additionally, a more detailed comparison of PEC immunosensors with respect to controlled-release strategies is provided in the SM.

3.5. Stability, selectivity, and reproducibility of the split-type PEC immunosensor

Stability, selectivity, and reproducibility are important indicators of the application prospects of a sensor [46–48]. As shown in Fig. 6 C, to investigate the selectivity of a specific sensor, the target detector NSE was selected using a mixture of three different detection markers: carcino-embryonic antigen (CEA), procalcitonin (PCT), and insulin. NSE antigens with a tested range of 1 ng mL^{-1} contained 100 ng mL^{-1} interferents. Next, three test substances that did not contain the NSE antigen on the empty electrode were incubated. Evidently, the split-type sensor exhibited excellent selectivity and specificity.

The stability of the sensor was judged by the fluctuation of the photocurrent under a continuous on/off light source cycle for 400 s Fig. 6D shows the change in the photocurrent in NSE with a test

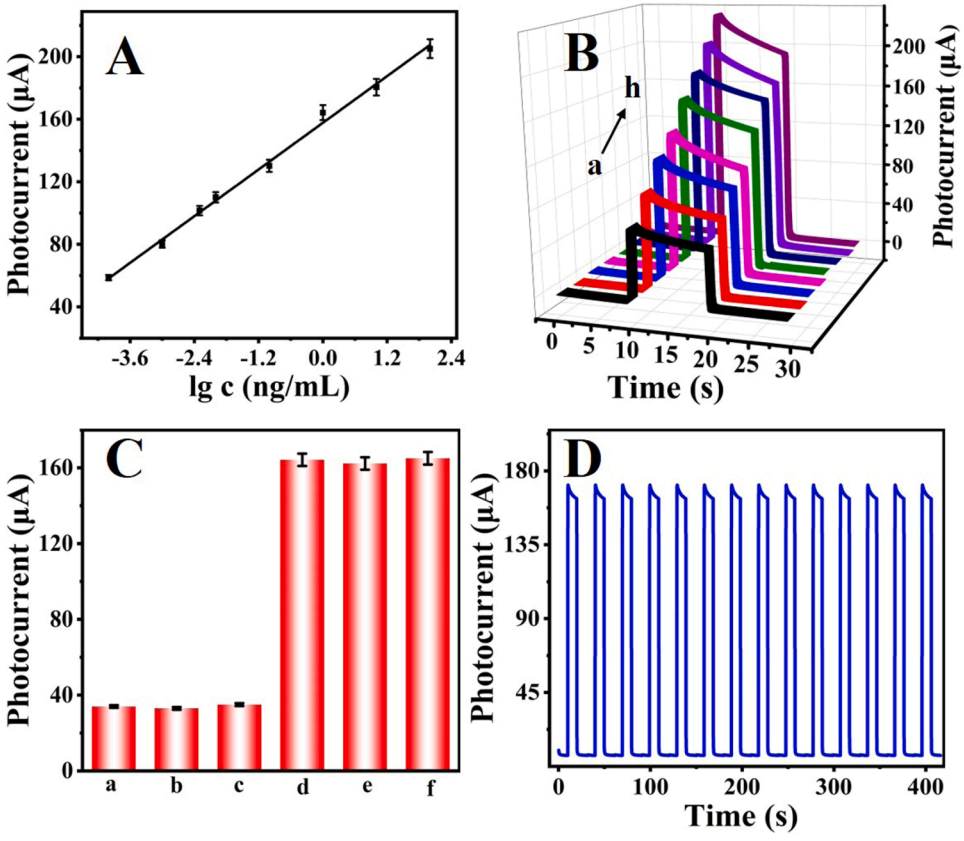

Fig. 6. (A) Detection of photocurrent response of target NSE with different concentrations. (B) Linear relationship between target concentration and photocurrent of PEC sensor for NSE detection: (a) 0.0001, (b) 0.001, (c) 0.005, (d) 0.01, (e) 0.1, (f) 1, (g) 10, and (h) 100 (ng mL^{-1}). (C) Split-type PEC sensor for testing the selectivity of NSE. (a) 100 ng mL^{-1} carcino-embryonic antigen (CEA); (b) 100 ng mL^{-1} procalcitonin (PCT); (c) 100 ng mL^{-1} insulin; (d) 1.0 ng mL^{-1} NSE + 100 ng mL^{-1} CEA; (e) 1.0 ng mL^{-1} NSE + 100 ng mL^{-1} PCT; (f) 1.0 ng mL^{-1} NSE + 100 ng mL^{-1} insulin. (D) Stability of split-type PEC immunosensor excited by light source from 0 to 400 s (c_{NSE} = 1.0 ng mL^{-1}). Error bars = SD ($n = 3$).

concentration of 1.0 ng mL^{-1}. Evidently, even if the light caused some photocorrosion to the electrode, the change in photocurrent was nearly negligible under the on/off light source for 400 s, thus indicating that the sensor has good stability. In addition, the storage stability of the sensor was explored and the photocurrent change of the sensor after storage at 4 °C for 1, 3, 5, 7, and 14 d was investigated (Fig. S11A). Evidently, the photocurrent was maintained at 97.72%, 96.42%, 95.31%, 93.75%, and 92.01%, respectively, thus suggesting satisfactory storage stability. The stability of the PEC sensor was measured at four different concentrations (10, 0.1, 0.01, and 0.001 ng mL^{-1}) in Fig. S10.

Reproducibility is an important indicator to evaluate the performance of this PEC immunosensor by varying the electrode environment to determine the performance of this sensor. To investigate the reproducibility, five sets of immunosensors containing 1.0 ng mL^{-1} NSE under the same conditions were selected (Fig. S11B). The relative standard deviation (RSD) was approximately 3.14%, which could be explained by the outstanding reproducibility of the PEC immunosensor.

3.6. Analysis of human serum sample

To evaluate the feasibility and accuracy of the constructed split-type PEC immunosensor for clinical diagnosis, actual sample assays were performed. As presented in Table S4, a series of spiked NSE samples with concentrations ranging from 0.75 to 5.11 ng mL^{-1} were mixed with different concentrations of NSE; the RSD values ranged from 1.7% to 3.1%, and the recoveries ranged from 97.60% to 103.7%. Therefore, this split-type PEC sensor exhibited good results in the detection of NSE in human serum samples and is promising for future applications.

4. Conclusion

In conclusion, a split-type PEC immunosensor was successfully constructed for the detection of NSE by separating the immunization process from a 96-well plate using an ITO/In_2O_3/$BiVO_4$/ZIF-8 working electrode. The $BiVO_4$ film, successfully adsorbed onto In_2O_3 using the s-SILAR method, formed a heterogeneous structure to accelerate the separation of photogenerated electron-hole pairs, accelerated the electron transfer, and formed a satisfactory photocurrent. Furthermore, the biological suitability of ZIF-8 hindered electron transfer and isolated biomolecules from direct contact with inorganic materials. By releasing gluconic acid, the split-type PEC sensor exploited the pH-sensitive property of the ZIF-8 protective layer to achieve sensitive detection of NSE by detecting changes in the concentration of NSE. The detection range was between 0.1 pg mL^{-1} to 100 ng mL^{-1} with a detection limit as low as 0.03 pg mL^{-1}; evidently, it exhibited excellent stability and selectivity. In summary, the split-type PEC immunosensor introduced in this study achieved the highly sensitive detection of NSE, thus presenting as a novel method for future biological disease detection.

CRediT authorship contribution statement

Yu Bai: Conceptualization, Data curation, Writing – original draft. **Dongquan Leng**: Methodology, Data curation, Writing – review & editing. **Tao Feng**: Methodology. **Xuan Kuang**: Formal analysis. **Dawei Fan**: Methodology, Writing – review & editing. **Yuyang Li**: Methodology, Supervision. **Xiang Ren**: Funding acquisition, Formal analysis. **Qin Wei**: Formal analysis, Writing – review & editing. **Huangxian Ju**: Formal analysis, Writing – review & editing.

Declaration of Competing Interest

The authors declare that they have no known competing financial interests or personal relationships that could have appeared to influence the work reported in this paper.

Data Availability

No data was used for the research described in the article.

Acknowledgments

This study was supported by the National Key Scientific Instrument and Equipment Development Project of China (No. 21627809), National Natural Science Foundation of China (No. 51904114), the Shandong Provincial Natural Science Foundation (No. ZR2020QB097), the Innovation Team Project of Colleges and Universities in Jinan (No. 2019GXRC027) and the Special Foundation for Taishan Scholar Professorship of Shandong Province.

Appendix A. Supporting information

Supplementary data associated with this article can be found in the online version at doi:10.1016/j.snb.2023.133479.

References

[1] Z. Yu, H. Gong, F. Xue, Y. Zeng, X. Liu, D. Tang, Flexible and high-throughput photothermal biosensors for rapid screening of acute myocardial infarction using thermochromic paper-based image analysis, Anal. Chem. 94 (2022) 13233–13242.
[2] J. Xu, R. Zeng, L. Huang, Z. Qiu, D. Tang, Dual-signaling photoelectrochemical biosensor based on biocatalysis-induced vulcanization of Bi_2MoO_6 nanosheets, Anal. Chem. 94 (2022) 11441–11448.
[3] L. Huang, G. Cai, R. Zeng, Z. Yu, D. Tang, Contactless photoelectrochemical biosensor based on the ultraviolet-assisted gas sensing interface of three-dimensional SnS(2) nanosheets: from mechanism reveal to practical application, Anal. Chem. 94 (2022) 9487–9495.
[4] Y.X. Lai, L.J. Wang, Y. Liu, G.J. Yang, C.L. Tang, Y. Deng, S. Li, Immunosensors based on nanomaterials for detection of tumor markers, J. Biomed. Nanotechnol. 14 (2018) 44–65.
[5] W.W. Tu, Z.Y. Wang, Z.H. Dai, Selective photoelectrochemical architectures for biosensing: design, mechanism and responsibility, Trends Anal. Chem. 105 (2018) 470–483.
[6] M.X. Jia, X.F. Liao, L. Fang, B.Y. Jia, M. Liu, D.H. Li, L.D. Zhou, W. j Kong, Recent advances on immunosensors for mycotoxins in foods and other commodities, Trends Anal. Chem. 136 (2021), 116193.
[7] Y. Gao, Y. Zeng, X. Liu, D. Tang, Liposome-mediated in situ formation of type-i heterojunction for amplified photoelectrochemical immunoassay, Anal. Chem. 94 (2022) 4859–4865.
[8] Z. Yu, H. Gong, J. Xu, Y. Li, Y. Zeng, X. Liu, D. Tang, Exploiting photoelectric activities and piezoelectric properties of $NaNbO_3$ semiconductors for point-of-care immunoassay, Anal. Chem. 94 (2022) 3418–3426.
[9] S. Ferraro, F. Braga, R. Luksch, M. Terenziani, S. Caruso, M. Panteghini, Measurement of Serum Neuron-Specific Enolase in Neuroblastoma: Is There a Clinical Role? Clin. Chem. 66 (2020) 667–675.
[10] X. Gao, P. Zheng, S. Kasani, S. Wu, F. Yang, S. Lewis, et al., Paper-based surface-enhanced raman scattering lateral flow strip for detection of neuron-specific enolase in blood plasma, Anal. Chem. 89 (2017) 10104–10110.
[11] L.M. van Veenendaal, E. Bertolli, C.M. Korse, W.M.C. Klop, M.E.T. Tesselaar, A.C. J. van Akkooi, The clinical utility of neuron-specific enolase (NSE) serum levels as a biomarker for merkel cell carcinoma (MCC), Ann. Surg. Oncol. 28 (2021) 1019–1028.
[12] K. Yan, P.K. Kannan, D. Doonyapisut, K.B. Wu, C.H. Chung, J.D. Zhang, Advanced functional electroactive and photoactive materials for monitoring the environmental pollutants, Adv. Funct. Mater. 31 (2021) 2008227.
[13] F. Yang, J.F. Xi, L.Y. Gan, Y.S. Wang, S.W. Lu, W.L. Ma, et al., Improved charge transfer and photoelectrochemical performance of CuI/Sb_2S_3/TiO_2 heterostructure nanotube arrays, J. Colloid Interface Sci. 464 (2016) 1–9.
[14] M. Chen, J. Guo, F.J. Mo, H. Meng, W.Q. Yu, Y.Z. Fu, Self-enhanced photoelectrochemical sensor based on a Schottky heterostructure organic electron donor matrix, ChemComm 58 (2022) 455–458.
[15] Y. Zhang, J.Q. Zhang, M.Y. Nie, K. Sun, C.H. Li, J.Q. Yu, Photoelectrochemical water splitting under visible light over anti-photocorrosive In_2O_3-coupling ZnO nanorod arrays photoanode, J. Nanopart. Res 17 (2015) 1–11.
[16] M. Meng, X.L. Wu, X.B. Zhu, L. Yang, Z.X. Gan, X.S. Zhu, L.Z. Liu, P.K. Chu, Cubic In_2O_3 microparticles for efficient photoelectrochemical oxygen evolution, J. Phys. Chem. Lett. 5 (2014) 4298–4304.
[17] S.Y. Yu, L. Zhang, L.B. Zhu, Y. Gao, G.C. Fan, D.M. Han, G.X. Chen, W.W. Zhao, Bismuth-containing semiconductors for photoelectrochemical sensing and biosensing, Coord. Chem. Rev. 393 (2019) 9–20.
[18] W.J. Jo, J.W. Jang, K.J. Kong, H.J. Kang, J.Y. Kim, H. Jun, et al., Phosphate doping into monoclinic bivo4 for enhanced photoelectrochemical water oxidation activity, Angew. Chem. Int. Ed. 51 (2012) 3147–3151.
[19] L.Y. Chen, W.D. Zhang, In_2O_3/g-C_3N_4 composite photocatalysts with enhanced visible light driven activity, Appl. Surf. Sci. 301 (2014) 428–435.

[20] K.K. Dey, S. Gahlawat, P.P. Ingole, BiVO4 optimized to nano-worm morphology for enhanced activity towards photoelectrochemical water splitting, J. Mater. Chem. A 7 (2019) 21207–21221.
[21] J. Mu, B. Chen, M. Zhang, Z. Guo, P. Zhang, Z. Zhang, et al., Enhancement of the visible-light photocatalytic activity of In_2O_3-TiO_2 nanofiber heteroarchitectures, ACS Appl. Mater. Interfaces 4 (2012) 424–430.
[22] J.Z. Yin, S.B. Huang, Z.C. Jian, M.L. Pan, Y.Q. Zhang, Z.B. Fei, et al., Enhancement of the visible light photocatalytic activity of heterojunction In_2O_3/$BiVO_4$ composites, Appl. Phys. A 120 (2015) 1529–1535.
[23] Z. Dai, J. Guo, C. Zhao, Z. Gao, Y.Y. Song, Fabrication of homochiral metal-organic frameworks in TiO_2 nanochannels for in situ identification of 3,4-dihydroxyphenylalanine enantiomers, Anal. Chem. 93 (2021) 11515–11524.
[24] X. Jian, J. Xu, Y. Wang, C. Zhao, Z. Gao, Y.Y. Song, Deployment of MIL-88B(Fe)/TiO_2 nanotube-supported Ti wires as reusable electrochemiluminescence microelectrodes for noninvasive sensing of H_2O_2 from single cancer cells, Anal. Chem. 93 (2021) 11312–11320.
[25] J. Guo, L. Yang, Z. Gao, C. Zhao, Y. Mei, Y.-Y. Song, Insight of MOF environment-dependent enzyme activity via MOFs-in-nanochannels configuration, ACS Catal. 10 (2020) 5949–5958.
[26] M.T. Wharmby, S. Henke, T.L. Bennett, C. Mellot-Draznieks, Y.Z. Yue, A. K. Cheetham, Structural flexibility in prototypical zeolitic imidazolate frameworks, Acta Crystallogr. A 71 (2015) S85–S86.
[27] X.C. Huang, Y.Y. Lin, J.P. Zhang, X.M. Chen, Ligand-directed strategy for zeolite-type metal-organic frameworks: zinc(II) imidazolates with unusual zeolitic topologies, Angew. Chem. Int. Ed. 45 (2006) 1557–1559.
[28] Q.Q. Wang, X.P. Zhang, L. Huang, Z.Q. Zhang, S.J. Dong, GOx@ZIF-8(NiPd) nanoflower: an artificial enzyme system for tandem catalysis, Angew. Chem. Int. Ed. 56 (2017) 16082–16085.
[29] E. Astria, M. Thonhofer, R. Ricco, W.B. Liang, A. Chemelli, A. Tarzia, et al., Carbohydrates@MOFs, Mater. Horiz. 6 (2019) 969–977.
[30] M.D. Velasquez-Hernandez, R. Ricco, F. Carraro, F.T. Limpoco, M. Linares-Moreau, E. Leitner, et al., Degradation of ZIF-8 in phosphate buffered saline media, Crystengcomm 21 (2019) 4538–4544.
[31] W.H. Chen, G.F. Luo, M. Vazquez-Gonzalez, R. Cazelles, Y.S. Sohn, R. Nechushtai, et al., Glucose-responsive metal-organic-framework nanoparticles act as "smart" sense-and-treat carriers, Acs Nano 12 (2018) 7538–7545.
[32] W. Liang, Z. Xie, J. Cheng, D. Xiao, Q. Xiong, Q. Wang, et al., A light-triggered pH-responsive metal-organic framework for smart delivery of fungicide to control sclerotinia diseases of oilseed rape, ACS Nano 15 (2021) 6987–6997.
[33] Y.R. Qian, J.H. Feng, R. Xu, D.W. Fan, Y. Du, X. Ren, et al., Zinc and molybdenum Co-Doped $BiVO_4$ nanoarray for photoelectrochemical diethylstilbestrol analysis based on the dual-competitive system of manganese hexacyanoferrate hydrate nanocubes, ACS Appl. Mater. Interfaces 12 (2020) 16662–16669.
[34] J.H. Feng, F.Y. Li, Y.R. Qian, X. Sun, D.W. Fan, H. Wang, H.M. Ma, Q. Wei, Mo-doped porous $BiVO_4$/Bi_2S_3 nanoarray to enhance photoelectrochemical efficiency for quantitative detection of 17 beta-estradiol, Sens. Actuators B Chem. 305 (2020), 127443.
[35] D.Q. Leng, J.S. Li, R. Xu, L. Liu, X.J. Liu, D.W. Fan, H. Wang, Q. Wei, H.X. Ju, THCH as electron donor in controlled-release system for procalcitonin analysis based on $Bi_2Sn_2O_7$ photoanode, Sens. Actuators B Chem. 321 (2020), 128509.
[36] R. Xu, L. Liu, X.J. Liu, Y.Y. Li, R.Q. Feng, H. Wang, D.W. Fan, D. Wu, Q. Wei, Novel electron donor encapsulation assay based on the split-type photoelectrochemical interface, ACS Appl. Mater. Interfaces 12 (2020) 7366–7371.
[37] C. Seong, P. Mane, H. Bae, S. Lee, S.H. Kang, S.W. Ryu, J.S. Ha, Simple fabrication of $BiVO_4$ thin films synthesized by modified silar method: effect of film thickness, J. Electrochem. Soc. 169 (2022), 016501.
[38] S. Zhou, J. Guo, Z. Dai, C. Liu, J. Zhao, Z. Gao, Y.Y. Song, Engineering homochiral MOFs in TiO_2 nanotubes as enantioselective photoelectrochemical electrode for chiral recognition, Anal. Chem. 93 (2021) 12067–12074.
[39] J. Xu, C. Zhao, K. Niu, Z. Gao, Y.Y. Song, Renewable photoelectrochemical cytosensing platform for rapid capture and detection of circulating tumor cells, Anal. Chim. Acta 1142 (2021) 1–9.
[40] W. Guo, D. Tang, O. Mabayoje, B.R. Wygant, P. Xiao, Y.H. Zhang, C.B. Mullins, A simplified successive ionic layer adsorption and reaction (s-SILAR) method for growth of porous $BiVO_4$ thin films for photoelectrochemical water, Oxid., J. Electrochem. Soc. 164 (2017) H119–H125.
[41] M. Meng, X. Wu, X. Zhu, X. Zhu, P.K. Chu, Facet cutting and hydrogenation of In_2O_3 nanowires for enhanced photoelectrochemical water splitting, ACS Appl. Mater. Interfaces 6 (2014) 4081–4088.
[42] J. Feng, N. Li, Y. Du, X. Ren, X. Wang, X.J. Liu, H.M. Ma, Q. Wei, Ultrasensitive double-channel microfluidic biosensor-based cathodic photo-electrochemical analysis via signal amplification of SOD-Au@PANI for cardiac troponin i detection, Anal. Chem. 93 (2021) 14196–14203.
[43] Z. Abbas, R.A. Soomro, N.H. Kalwar, M. Tunesi, M. Willander, S. Karakus, A. Kilislioğlu, In Situ growth of $CuWO_4$ nanospheres over graphene oxide for photoelectrochemical (PEC) immunosensing of clinical biomarker, Sensors 20 (2019) 148.
[44] R.A. Soomro, S. Jawaid, P. Zhang, X. Han, K.R. Hallam, S. Karakuş, A. Kilislioğlu, B. Xu, M. Willander, $NiWO_4$-induced partial oxidation of MXene for photo-electrochemical detection of prostate-specific antigen, Sens. Actuators B: Chem. 328 (2021), 129074.
[45] R.A. Soomro, N.H. Kalwar, A. Avci, E. Pehlivan, K.R. Hallam, M. Willander, In-situ growth of $NiWO_4$ saw-blade-like nanostructures and their application in photo-electrochemical (PEC) immunosensor system designed for the detection of neuron-specific enolase, Biosens. Bioelectron. 141 (2019), 111331.
[46] Z. Yu, H. Gong, Y. Li, J. Xu, J. Zhang, Y.Y. Zeng, X.L. Liu, D.P. Tang, Chemiluminescence-derived self-powered photoelectrochemical immunoassay for detecting a low-abundance disease-related protein, Anal. Chem. 93 (2021) 13389–13397.
[47] K. Zhang, S. Lv, Q. Zhou, D. Tang, CoOOH nanosheets-coated g-C_3N_4/$CuInS_2$ nanohybrids for photoelectrochemical biosensor of carcinoembryonic antigen coupling hybridization chain reaction with etching reaction, Sens. Actuators B: Chem. 307 (2020), 127631.
[48] Z. Luo, Q. Qi, L. Zhang, R. Zeng, L. Su, D. Tang, Branched polyethylenimine-modified upconversion nanohybrid-mediated photoelectrochemical immunoassay with synergistic effect of dual-purpose copper ions, Anal. Chem. 91 (2019) 4149–4156.

Yu Bai is a master student in school of chemistry and chemical engineering, University of Jinan. His current researches are photoelectrochemical sensor and nanomaterials.

Dongquan Leng is a master student in school of chemistry and chemical engineering, University of Jinan. His current researches are photoelectrochemical sensor and nanomaterials.

Tao Feng is a master student in school of chemistry and chemical engineering, University of Jinan. His current researches electrochemiluminescence sensor and nanomaterials.

Xuan Kuang obtained her Ph.D. in Analytical Chemistry in 2015. Her research interests focus on metal organic materials and their application in electrochemical sensors, and fundamental electrochemical studies of energy storage devices and synthetic nanomotors.

Dawei Fan her Ph. D degree from Lanzhou Institute of Chemical Physics, Chinese Academy of Sciences. She is currently an associate professor at University of Jinan. Her main research interests include electrochemical sensors and photoelectrochemical sensors. She has published over 50 papers.

Yuyang Li received his Ph.D. degree from China University of Petroleum (East China) in 2018. His main research interest are the design and preparation of functional nanomaterial, sensor technology, fluorescence imaging, and their industrial application. He has been hosting one national scientific research project.

Xiang Ren received his B.S. degree in Chemistry of Materials from University of Jinan in 2012, M.S. degree in Chemical Engineering and Technology from University of Jinan in 2015 and Ph.D. degree from University of Jinan/University of Electronic Science and Technology of China in 2019. Now, he is an associate professor in University of Jinan. His main research interests are energy catalysis, nanomaterials controlled-synthesis, and electrochemical biosensors.

Qin Wei, a professor and DSc, has devoted herself to analytical teaching and scientific research. Her main research interests are the determination of protein and nucleic acid by photometry and the electrochemical immunosensor preparation. She has published over 200 articles on analysis, immunosensor and applied successfully for many research projects, such as Analytical Chemistry, Advanced Functional Materials, Chemical Communication, Biosensors & Bioelectronics, Journal of Materials Chemistry A, and ACS Applied Materials & Interfaces.

Huangxian Ju, received his BS, MS and Ph.D. degrees from Nanjing University during 1982–1992. He was a postdoc in Montreal University (Canada) from 1996 to 1997 and a guest professor in three universities of Germany and Ireland in 1999–2000. He became an associate and full professor of Nanjing University in 1993 and 1999. He is currently the director of State Key Laboratory of Analytical Chemistry for Life Science. His research interests focus on analytical biochemistry, biosensing and molecular diagnosis. He has published 13 books and 790 papers in different journals with SCIE h-index of 100 (>38000 citations) and Google Scholar h-index of.110 (> 44000 citations).